Energy Advances

ROYAL SOCIETY OF CHEMISTRY

PAPER

View Article Online
View Journal

Open Access Article. Published on 13 February 2026. Downloaded on 2/25/2026 7:33:26 AM.
This article is licensed under a Creative Commons Attribution-NonCommercial 3.0 Unported Licence.

Check for updates

Cite this: DOI: 10.1039/d5ya00343a

Numerical investigation of highly efficient chlorine-doped perovskite solar cells

Md Abdul Kuddus Sheikh,* Md. Shazarul Islam and Hasina Huq*

Received 24th November 2025,
Accepted 8th February 2026

DOI: 10.1039/d5ya00343a

rsc.li/energy-advances

In this study, we present a comprehensive numerical investigation of chlorine-doped perovskite solar cells using the SCAPS-1D simulation framework, with the device structure ITO/ZnO/$CH_3NH_3PbI_{3-x}Cl_x$/NiO_x/Au. This work focuses on optimizing active-layer properties and compositional engineering to enhance photovoltaic performance. Initially, the influence of absorber thickness on device parameters was investigated, revealing that $CH_3NH_3PbI_3$ achieves optimal performance at 800 nm thickness, delivering a power conversion efficiency (PCE) of 24.17%, along with a short circuit current density (J_{sc}) of 25.31 mA cm^{-2}, an open circuit voltage (V_{oc}) of 1.15 V, and a fill factor (FF) of 82.75%. Subsequently, chlorine incorporation was systematically varied to evaluate its effect on device performance. The composition $MAPbI_{2.8}Cl_{0.2}$ emerged as the most favorable, achieving an enhanced PCE of 27.34%, with J_{sc} = 25.00 mA cm^{-2}, V_{oc} = 1.31 V, and FF = 83.63%. Finally, comparative simulations across different electron transport layers, hole transport layers, absorber materials, and lead-free perovskites highlight the performance advantages of an optimized structure. Our simulated results provide valuable insights into the design of highly efficient Cl-doped perovskite solar cells and demonstrate the potential of compositional tuning for next-generation photovoltaic devices.

Introduction

Solar cells (SCs) play an essential role in future renewable energy systems by converting solar irradiation into electrical power with high efficiency and continuously decreasing production cost. Conventional crystalline silicon (Si) SCs dominate the current photovoltaic (PV) market, having achieved certified power conversion efficiencies (PCEs) of nearly 26% under standard illumination.[1–4] Nevertheless, Si technology is limited by its theoretical single-junction Shockley–Queisser efficiency limit (~33%) and faces challenges such as energy-intensive fabrication, high capital expenditure, and limited opportunities for low-temperature or flexible processing.[5] These constraints have stimulated strong interest in emerging PV materials capable of offering high efficiency, tunable optoelectronic properties, low-cost production, and compatibility with scalable deposition methods.[6–8]

Metal halide perovskite solar cells (PSCs) have rapidly advanced over the past decade, driven by their remarkable properties including high absorption coefficients, long carrier lifetimes, low defect formation energies, and facile solution processing.[9–12] Organic–inorganic lead halide perovskites, particularly methylammonium lead iodide ($MAPbI_3$, MA = $CH_3NH_3^+$), have achieved PCEs exceeding 26%, rivaling Si while offering substantially lower processing temperatures.[1] Although $MAPbI_3$ possesses outstanding light-harvesting properties, its practical deployment is limited by instability arising from defects and environmental exposure; compositional engineering such as halide incorporation can reduce defect densities and enhance intrinsic stability, complementing external passivation and encapsulation approaches.[13,14] To overcome instability concerns, several studies have investigated compositional and interfacial engineering strategies.[15,16] Advanced approaches, including humidity-assisted crystallization, surface passivation, and robust encapsulation, have been shown to suppress phase transitions and alleviate environmental degradation. The main toxicity issue associated with $MAPbI_{3-x}Cl_x$ absorbers arises from potential lead release during degradation, which can be substantially reduced through effective encapsulation, lead-trapping strategies, and appropriate end-of-life recycling practices.[17,18] For example, Wang *et al.* demonstrated that controlled humidity-assisted crystallization stabilizes cubic $CsPbI_3$ by promoting larger grain sizes and reducing halide vacancy defects.[19] Similarly, Jiang *et al.* employed polymer–barrier encapsulation to dramatically suppress lead leakage and external degradation pathways, enabling long-term outdoor stability.[20] These works highlight the importance of defect reduction, interface control, and environmental barrier strategies for achieving durable PSC performance. Another major research direction involves halide and compositional engineering as a

Department of Electrical and Computer Engineering, The University of Texas Rio Grande Valley, 1201 West University Dr, Edinburg, TX, 78539, USA.
E-mail: mdabdul.kuddussheikh@utrgv.edu, hasina.huq@utrgv.edu, mdshazarul.islam01@utrgv.edu

Open Access Article. Published on 13 February 2026. Downloaded on 2/25/2026 7:33:26 AM.
This article is licensed under a Creative Commons Attribution-NonCommercial 3.0 Unported Licence.

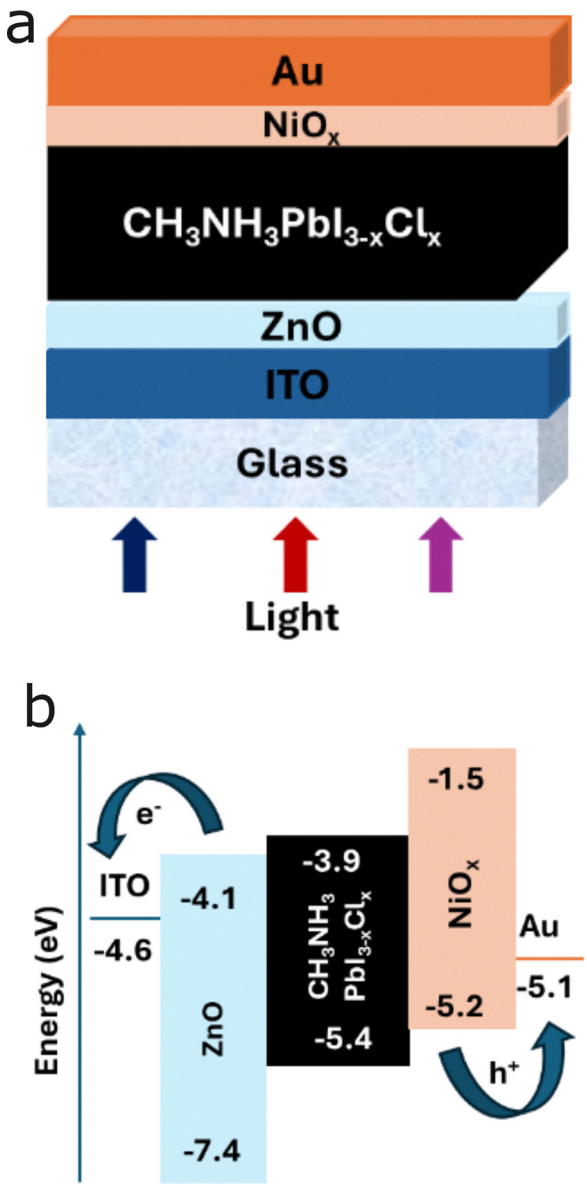

Fig. 1 (a) Schematic diagram of the planar n–i–p solar cell configuration (ITO/ZnO/$CH_3NH_3PbI_{3-x}Cl_x$/NiO_x/Au) and (b) energy level diagram of the device.

means of improving device efficiency through improved crystallinity, defect passivation, and voltage enhancement.[15,16] Chloride incorporation has been widely reported to prolong carrier lifetime, enhance the built-in electric field, and suppress non-radiative recombination; moreover, while encapsulation is essential for mitigating extrinsic degradation in $MAPbI_3$-based solar cells, chlorine incorporation effectively passivates bulk and interfacial defects, improves carrier diffusion lengths, and suppresses ion migration, thereby contributing to improved intrinsic stability in addition to enhanced device performance.[21,22] Chen *et al.* showed that trace levels of chloride significantly suppress non-radiative recombination and increase open circuit voltage (V_{oc}) by modulating the electronic structure and passivating defects.[21] Stone *et al.* elucidated that a Cl-containing precursor phase can slow down crystallization, resulting in denser films and higher crystal quality that favor improved charge transport and reduced recombination.[22] Despite these advances, the quantitative influence of chloride content on V_{oc}, short circuit current density (J_{sc}), and fill factor (FF), and its interplay with ETL/HTL energetics remains insufficiently understood, especially in computational design frameworks that can isolate individual parameters.

In this study, we conduct a comprehensive numerical investigation of chlorine-doped $MAPbI_{3-x}Cl_x$ perovskite SCs using the SCAPS-1D device simulation platform, focusing on the architecture ITO/ZnO/$MAPbI_{3-x}Cl_x$/NiO_x/Au. First, the $MAPbI_3$ absorber thickness was optimized, with 800 nm identified as the ideal thickness enabling a PCE of 24.17% (V_{oc} = 1.15 V, J_{sc} = 25.31 mA cm^{-2}, and FF = 82.75%). We then systematically investigated chloride incorporation, revealing that $MAPbI_{2.8}Cl_{0.2}$ yields significantly enhanced device performance with a PCE of 27.34%, driven by improved V_{oc} (1.31 V) and FF (83.63%). These results are consistent with experimental observations by Chen *et al.* and Hieulle *et al.*, who demonstrated that halide substitution and defect-suppression strategies can dramatically elevate V_{oc} and device stability.[15,21] Finally, comparative simulations incorporating alternative electron transport layers (ETLs), hole transport layers (HTLs), and absorber materials highlight the superior performance of an optimized ZnO/$MAPbI_{2.8}Cl_{0.2}$/NiO_x configuration relative to conventional PSC structures. Collectively, this work provides important insights

Table 1 Physical parameters of the materials used in the proposed solar cell simulated devices

Parameters	Layer			
	NiO_x (HTL)[39,40]	$MAPbI_3$ (absorber)[25,41]	ZnO (ETL)[26,42]	ITO[43,44]
Thickness (nm)	20	800	20	100
Band gap (eV)	3.8	1.55	3.3	3.5
Electron affinity (eV)	1.5	3.8	4.1	4.0
Relative permittivity	10.7	10	9.0	9.0
Conduction band effective density of states (cm^{-3})	2.8×10^{19}	2.8×10^{18}	4.0×10^{18}	2.2×10^{18}
Valence band effective density of states (cm^{-3})	10^{19}	3.9×10^{18}	1.0×10^{19}	1.8×10^{19}
Electron mobility ($cm^2\ V^{-1}\ s^{-1}$)	12	10	100	30
Hole mobility ($cm^2\ V^{-1}\ s^{-1}$)	2.8	10	25.0	5.0
Shallow donor density (cm^{-3})	0	10^{14}	1×10^{16}	2×10^{20}
Shallow acceptor density (cm^{-3})	10^{18}	—	0	0
Defect density (cm^{-3})	1×10^{14}	3×10^{14}	1×10^{14}	1×10^{14}

 © 2026 The Author(s). Published by the Royal Society of Chemistry

Open Access Article. Published on 13 February 2026. Downloaded on 2/25/2026 7:33:26 AM.
This article is licensed under a Creative Commons Attribution-NonCommercial 3.0 Unported Licence.

Table 2 Physical parameters of the materials using various chlorine doped perovskite layers

Parameters	Absorber layer					
	$MAPbI_3$[25,41]	$MAPbI_{2.8}Cl_{0.2}$[16,44]	$MAPbI_{2.4}Cl_{0.6}$[14,15]	$MAPbI_2Cl$[46,47]	$MAPbICl_2$[47]	$MAPbCl_3$[46,48]
Thickness (nm)	800	800	800	800	800	400
Band gap (eV)	1.55	1.57	1.59	2.09	2.58	2.88
Electron affinity (eV)	3.8	3.8	3.8	3.8	3.8	3.9
Relative permittivity	10	6.5	6.5	30	28	15
Conduction band effective density of states (cm^{-3})	2.8×10^{18}	2.2×10^{18}	2.2×10^{18}	2.0×10^{18}	2.0×10^{18}	3.5×10^{25}
Valence band effective density of states (cm^{-3})	3.9×10^{18}	1.8×10^{19}	1.8×10^{19}	1.0×10^{19}	1.0×10^{19}	3.5×10^{20}
Electron mobility ($cm^2\ V^{-1}\ s^{-1}$)	10.0	2.0	2.0	3.5	3.2	2.9
Hole mobility ($cm^2\ V^{-1}\ s^{-1}$)	10.0	2.0	2.0	3.5	3.2	24.5
Shallow donor density (cm^{-3})	10^{14}	10^{13}	10^{13}	10^{13}	10^{13}	10^{13}
Defect density (cm^{-3})	3×10^{14}	10^{13}	10^{13}	2×10^{14}	10^{14}	10^{13}

into halide engineering as a mechanism for boosting PV performance and underscores the critical role of controlled chloride incorporation in designing next-generation, high-efficiency perovskite SCs.

Materials and methodology

Device structure and modeling

Numerical simulations of planar perovskite-based solar cells were performed with one dimensional code SCAPS-1D, which is used to determine current density *vs.* voltage characteristics, energy band diagram, quantum efficiencies/spectral response, functional parameters (V_{oc} J_{sc}, FF, and PCE), total recombination currents, alternating current quantities and electron/hole densities and was designed by a team at the Department of Electronics and Information's Systems of the University of Ghent in Belgium.[23] The software utilizes one-dimensional Poisson and carrier continuity equations for electrons and holes.[23] Although SCAPS-1D assumes one-dimensional uniform layers, idealized defect distributions, and simplified recombination mechanisms (SRH, radiative, and Auger), with interface defects treated as discrete energy levels affecting carrier recombination and transport, the simulations were performed using convergence settings – including iteration tolerances for current and voltage, maximum iteration limits, and appropriate mesh resolution – to ensure stable and accurate solutions. These results were validated against reported experimental trends of chlorine-doped $MAPbI_3$ devices, showing qualitative agreement in key photovoltaic performance metrics. The physical parameters of each device layer can be systematically modified and optimized to achieve the most favorable performance characteristics, that include the layer thickness, bandgap, donor concentration and electron affinity to name just a few. A detailed sensitivity analysis of the current cell architecture, which could identify the most critical parameters influencing performance, is suggested as an important direction for future studies. At the time of this study, the latest and most up to date version of SCAPS was used, SCAPS 3.3.1.2. This simulation solves numerically the three basic semiconductor equations: the Poisson equation and continuity equations for holes and electrons.[24–26]

A schematic of the proposed device (ITO/ZnO/$MAPbI_{3-x}Cl_x$/NiO_x/Au) and the SC energy band diagram are shown in Fig. 1(a) and (b). The device is modeled with a simple equivalent circuit of resistances, a diode, and capacitances as in the equation $\tau = R \times C$, where the *RC* time constants describe charge relaxation and help understand carrier transport and

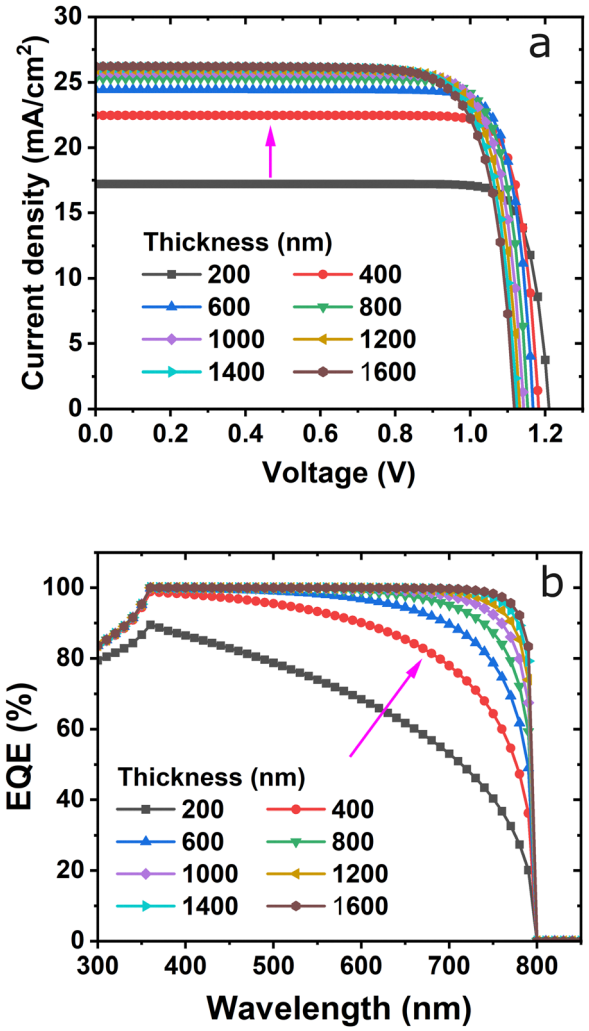

Fig. 2 Effect of absorber layer thickness on (a) *J*–*V* characteristics and (b) external quantum efficiency, keeping the ETL and HTL thickness fixed.

Open Access Article. Published on 13 February 2026. Downloaded on 2/25/2026 7:33:26 AM.
This article is licensed under a Creative Commons Attribution-NonCommercial 3.0 Unported Licence.

recombination. The simulations for the proposed device were run at a temperature of 300 K and under an illumination of AM 1.5G from the side of the device with the glass substrate. On the illuminated side, there is a transparent conducting oxide indium doped tin oxide (ITO) electrode which has a work function of 4.6 eV, while on the non-illuminated side a gold metal electrode with a work function of 5.1 eV was used.[27,28] NiO_x acts as the HTL (p-type), facilitating hole extraction, and ZnO acts as the ETL (n-type), enabling electron extraction. The central layer, $MAPbI_{3-x}Cl_x$ (x = 0, 0.2, 0.6, 1.0, 2.0), is a perovskite material responsible for light absorption and charge generation. The various input parameters for the layers which were gathered from the literature are presented in Tables 1 and 2. The expected results are the cell performance parameters such as J_{sc}, V_{oc}, FF, PCE, and external quantum efficiency (EQE).

Results and discussion

Fig. 1(a) shows the device with the n–i–p planar structure. The n-region is the ETL, the i region is the perovskite layer, and the p-region is the HTL. When the cell is subjected to light, excitons are mainly created in the perovskite i-region and then electrons move toward the n-layer ZnO, and holes move to the p-layer NiO_x as shown in the energy band diagram in Fig. 1(b). Dissociation of excitons as well as migration of electrons and holes are favored by electrical fields between the ETL and HTL. The work functions of ITO (used as a front contact) and Au (used as a back contact) were −4.6 eV and −5.1 eV, respectively.[27,28] The lowest unoccupied molecular orbital (LUMO) levels and the highest occupied molecular orbital (HOMO) levels of ZnO, $MAPbI_{3-x}Cl_x$, and NiO_x were −4.1 eV, −3.9 eV, and −1.5 eV and −7.4 eV, −5.4 eV, and −5.2 eV, respectively.[16,26,29,30] Through this proposed energy band alignment, the electrons and holes generated in the $MAPbI_{3-x}Cl_x$ absorption layer can efficiently move to the ITO electrode and Au electrode, respectively. The thickness of the active layer plays an important role in the device's performance. It can enhance absorption, which affects positively the J_{sc} and PCE.[31–33] Fig. 2(a) shows current density *vs.* voltage characteristics using the same fixed HTL and ETL thicknesses of 20 nm. The curve shows that the current increases from 200 nm to 600 nm and then slowly increases. On the other hand, the V_{oc} decreases with an increase in thickness. The thickness of the active layer varied from 200 nm to 1600 nm and the EQE is shown in Fig. 2(b). As can be observed from the spectra, in the wavelength range from 300–900 nm, the EQE values are almost similar up to 450 nm and then increase with active layer thicknesses. This consistency trend is because of the incident photons energy being lower than the active layer. The EQE reaches a maximum range from 360–650 nm wavelength except 600 nm which is highly favorable for the device's performance.

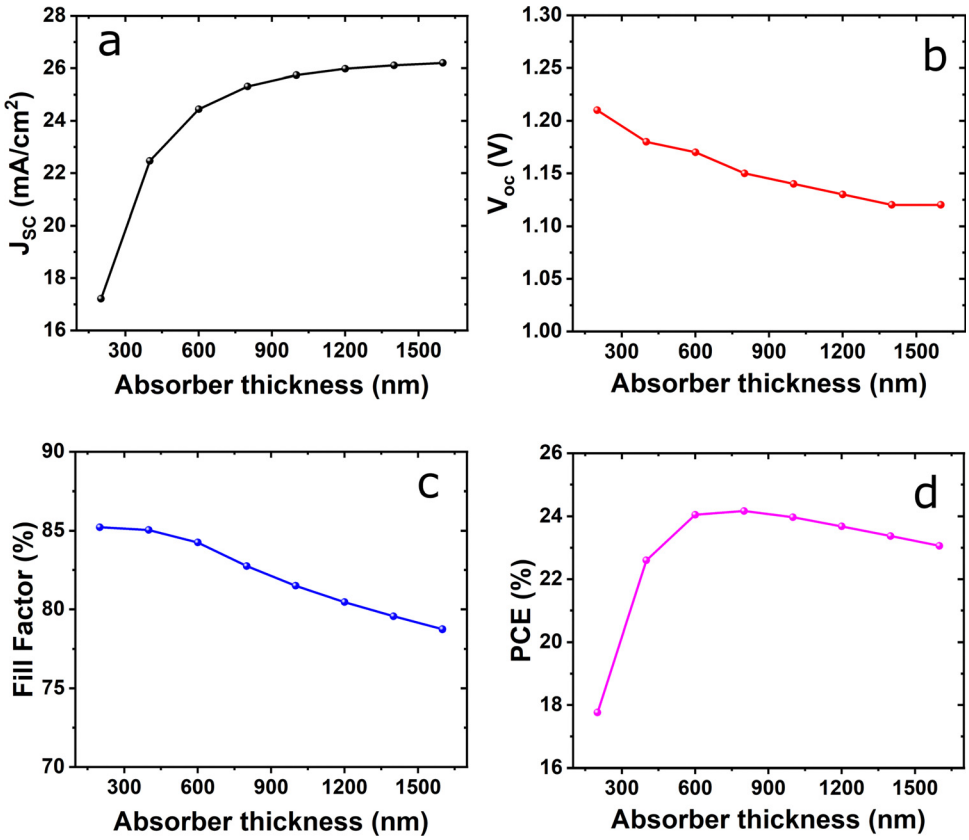

Fig. 3 Effect of absorber layer thickness on (a) J_{sc}; (b) V_{oc}; (c) fill factor; and (d) PCE, keeping the ETL and HTL thickness fixed.

 © 2026 The Author(s). Published by the Royal Society of Chemistry

Open Access Article. Published on 13 February 2026. Downloaded on 2/25/2026 7:33:26 AM.
This article is licensed under a Creative Commons Attribution-NonCommercial 3.0 Unported Licence.

The most significant change with the EQE values occurs in the wavelength range of 300–360 nm where in comparison to the thinner layers the thicker layers of $MAPbI_3$ have a much lower EQE value. This is a result of the active layer parasitic absorption which occurs because of the increased active layer thickness thereby decreasing the number of photons.

Furthermore, the impact of the active layer on device performance was examined as can be seen in Fig. 3. There is an increase of J_{sc} from 17.21 mA cm^{-2} to 26.20 mA cm^{-2} with the perovskite thickness as shown in Fig. 3(a) because of the higher photo generated carriers, which are dependent on the absorber layer thickness due to the improved light absorption capabilities.[34,35] For V_{oc}, it decreases with increasing thickness of the active layer as shown in Fig. 3(b). This is due to both the increase of dark saturation current and the increase of carrier recombination rate.[36] From Fig. 3(b), it is evident that the highest values were recorded when the thickness is 200 nm, which then slightly decrease with a change in the perovskite layer thickness. However, when examining raw data, the maximum V_{oc} (1.21 V) is achieved only when the perovskite layer is 200 nm. The V_{oc} slightly decreases for larger thickness, though the difference between the highest and lowest V_{oc} is only 7%. The primary reason for the varying V_{oc} with the absorber layer thickness could be an increase in the cells series resistance and a reduction in the photocurrent, both of which are related to the increase in the rate of carrier recombination.[37,38]

From the FF plot (Fig. 3(c)) it is noted that the maximum FF of 85.22% was observed at a lower thickness of 200 nm, which gradually decreased to 78.74%. The decrease in the FF is a result of the perovskite layers with increased thickness being greater than the diffusion length. This results in photogenerated carriers undergoing recombination in the quasi-neutral region. The device's PCE steadily improved with the increased thickness of the active layer reaching a maximum of 24.17% at 800 nm thickness and then decreases to 23.06% at 1600 nm as shown in Fig. 3(d). This increase occurs because if the active layer is too thin, it cannot efficiently collect electrons from the absorbing layer of the device.[45] However, the increase of active layer thickness exhibits a decrease in the PCE this decline in PCE is attributed to fewer photo-generated carriers. Finally, an increase in PCE until optimum thickness is due to the absorption of more photons by the active layer, which consequently generates more charge carrier concentration.

Doping is one of the most important processes in solar cell manufacturing to boost the efficiency of the devices. Especially, chlorine dopant contents in the absorber layer have an important effect on the performance of the devices. In simulating the device to analyze the effect of the chlorine dopant, a sample cell with an 800 nm absorber was used as optimized for the $MAPbI_3$ absorber layer. The remaining parameters are the same for the HTL and ETL as those listed in Table 2. As the chlorine content increases, the band gap increases from 1.55 eV to 2.88 eV for $MAPbI_3$ and $MAPbCl_3$, respectively.[41,46] Fig. 4 shows current density *vs.* voltage characteristics and EQE using the same fixed HTL and ETL thicknesses of 20 nm as a variable of the chlorine

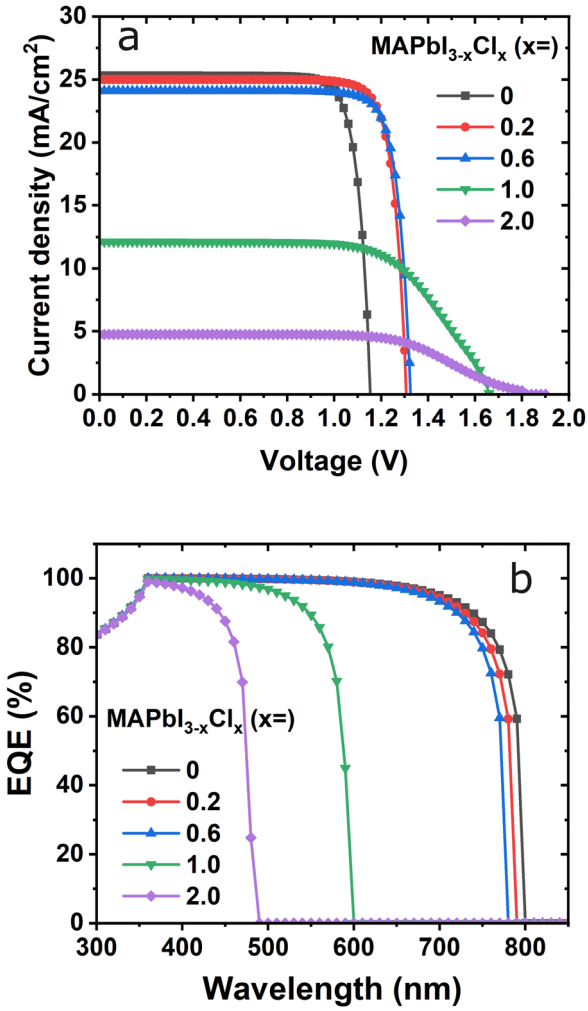

Fig. 4 Effect of chlorine-doped to $MAPbI_3$ on (a) J–V characteristics and (b) external quantum efficiency, keeping absorber, ETL and HTL layer thickness fixed.

dopant with iodine based perovskites. The curve in Fig. 4(a) shows that the current decreases slightly from 0 to 0.6 in $MAPbI_{3-x}Cl_x$ composition and then rapidly decreases. On the other hand, the V_{oc} increases with increases in dopant contents as this might be due to the band gap increases as shown in Table 2.

The chlorine dopant of the perovskite layer varied from 0 to 2 molar composition and the EQE is shown in Fig. 4(b). As can be seen from the spectra, in the wavelength range from 300–800 nm, the EQE values are almost similar up to 700 nm, except for the high dopant (>1.0). The EQE reaches a maximum range from 360–650 nm wavelength except for high dopant which is highly favorable for the device's performance. The most significant change with the EQE values occurs for over 1.0 composition and the EQE spectrum range decreases from 800 nm to 495 nm. This is a result of the low absorption which occurs because of the increased band gap thereby decreasing the number of photons. The EQE shows consistency with the J–V characteristics as shown in Fig. 4(a).

Open Access Article. Published on 13 February 2026. Downloaded on 2/25/2026 7:33:26 AM.
This article is licensed under a Creative Commons Attribution-NonCommercial 3.0 Unported Licence.

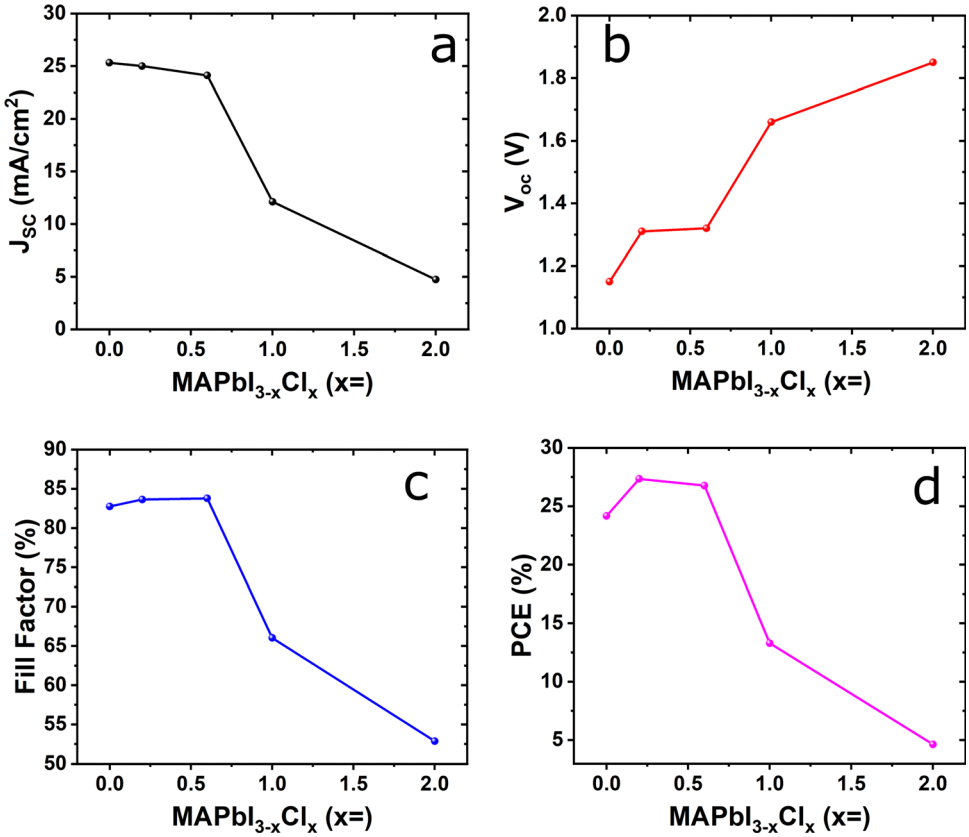

Fig. 5 Effect of chlorine-doped to $MAPbI_3$ on (a) J_{sc}; (b) V_{oc}; (c) fill factor; and (d) PCE, keeping absorber, ETL and HTL layer thickness fixed.

Fig. 5 provides the calculated device performance as a function of chlorine dopant with iodine-based perovskites. In Fig. 5(a and b), the J_{sc} decreases from 25.31 mA cm^{-2} to 4.74 mA cm^{-2}, which is 81% low, and the V_{oc} constantly increases from 1.15 V to 1.85 V which is 38% high. In terms of the FF, the value rapidly decreases from 82.75% to 52.86% for pure iodine to 2.0 chloride composition based $MAPbI_{3-x}Cl_x$ devices which is 36% low as shown in Fig. 5(c). In addition, as shown in Fig. 5(d), in the lower range of dopant contents (<0.6), the efficiency significantly decreases from 24.17% to 4.63% and the maximum efficiency is observed 27.34% at $MAPbI_{2.8}Cl_{0.2}$ composition. Nevertheless, the overall decline of the PCE continues after the optimum dopant. Based on Fig. 4(a), the device shows better performance for a low concentration of the dopants in the absorber, compared to the highly doped absorber. The sharp decline in J_{sc} for Cl concentrations >0.6 is due to bandgap widening that reduces visible light absorption and the potential formation of lattice strain or defect states that enhance non-radiative recombination. This behavior arises because excessive dopant concentrations reduce carrier lifetime; while low-level chlorine incorporation in $MAPbI_3$ effectively passivates defects and enhances carrier transport, excessive halide substitution widens the bandgap and lowers absorption, indicating the presence of an optimal doping range rather than a monotonic improvement in performance. On the other hand, the $MAPbCl_3$ based device shows a similar trend as simulated by other research groups even though they did not use NiO_x as a HTL in their simulated structure.[46] They obtained a PCE of 3.53% with J_{sc} = 9.78 mA cm^{-2}, V_{oc} = 1.99 V, and FF = 18.13%.

A comparison of our simulated results with previously reported Pb-based and Pb-free perovskite devices is summarized in Table 3. Our results clearly highlight an exceptional performance achieved through chloride incorporation in the $ZnO/MAPbI_{3-x}Cl_x/NiO_x$ architecture. Conventional $MAPbI_3$ SCs using transport layers such as ZnO/Cu_2O, spiro-MeOTAD, SnO_2, or TiO_2-typically deliver efficiencies in the range of 21–23%, with J_{sc} approximately 24 mA cm^{-2}, V_{oc} near 1.0–1.1 V and FF around 82–85%.[26,49] In contrast, our undoped $MAPbI_3$ device already exceeds many of these benchmarks with a PCE of 24.17%, and moderate chloride doping ($MAPbI_{2.8}Cl_{0.2}$ and $MAPbI_{2.4}Cl_{0.6}$) further elevates performance by substantially increasing the V_{oc} from 1.15 V to 1.32 V while maintaining high J_{sc} and FF. This leads to a record PCE of 27.34%, surpassing not only standard Pb-based $MAPbI_3$ devices but also those employing costly hole transport materials. These improvements reflect the strong influence of optimized chloride incorporation in suppressing non-radiative recombination, enhancing crystallinity, and improving interfacial charge extraction. Although excessive chloride addition leads to poorer performance due to phase segregation and reduced carrier mobility, an optimized Cl ratio clearly establishes an effective

 © 2026 The Author(s). Published by the Royal Society of Chemistry

Open Access Article. Published on 13 February 2026. Downloaded on 2/25/2026 7:33:26 AM.
This article is licensed under a Creative Commons Attribution-NonCommercial 3.0 Unported Licence.

Table 3 Comparison of the device performance obtained from simulations

Device structure	V_{oc} (V)	J_{sc} (mA cm^{-2})	FF (%)	PCE (%)	Ref.
ZnO/$MAPbI_3$/NiO_x	1.15	25.31	82.75	24.17	This work
ZnO/$MAPbI_{2.8}Cl_{0.2}$/NiO_x	1.31	25.00	83.63	27.34	This work
ZnO/$MAPbI_{2.4}Cl_{0.6}$/NiO_x	1.32	24.11	83.77	26.77	This work
ZnO/$MAPbI_2Cl$/NiO_x	1.66	12.11	66.03	13.29	This work
ZnO/$MAPbICl_2$/NiO_x	1.85	4.74	52.86	4.63	This work
ZnO/$MAPbCl_3$	1.99	9.78	18.13	3.53	46
ZnO/$MAPbI_3$/Cu_2O	1.1	24.5	84.8	23.21	26
ZnO/$MAPbI_3$/Spiro-MeOTAD	1.1	24.4	82.6	21.73	26
SnO_2/$MAPbI_3$/Spiro-MeOTAD	1.0	24.4	82.6	21.35	26
TiO_2/$MAPbI_3$/Spiro-MeOTAD	1.0	24.4	83.0	21.37	26
TiO_2/$MAPb_{1-x}Eu_xI_3$/Cu_2O	1.02	20.8	87.7	15.70	49
ZnO/$MAGeI_3$/Cu_2O	1.40	18.93	84.92	22.52	50
ZnO/$FAGeI_3$/Cu_2O	0.76	12.26	64.91	7.83	51
ZnO/$CsSnI_3$/Spiro-MeOTAD	0.95	25.87	0.73	17.88	52
ZnO/$MASnI_3$/CuSCN	0.84	34.18	70.45	20.17	53,54
ZnO/$BaZrS_3$/CuSCN	13.92	1.38	43.24	8.28	55

window for achieving high voltage and efficiency within Pb-based perovskite systems.[16,46] Sensitivity analysis was performed for the standard device to evaluate the influence of key parameters on device performance. The results indicate that the optimized structure exhibits high efficiency and stable operational behavior, suggesting its strong potential for experimental realization.

Finally, we have compared our simulated results with the comparable device structure of Pb-free perovskites as active materials. The comparison with Pb-free perovskites – including Sn-, Ge-, and chalcogenide-based compositions – highlights the motivation of the study, showing that while $MAPbI_{3-x}Cl_x$ achieves high efficiency, Pb-free alternatives are pursued to reduce toxicity and improve environmental safety; however, these Pb-free devices still lag significantly in overall photovoltaic performance, underscoring the need for strategic materials engineering in future development. Sn-based perovskites, such as $MASnI_3$ and $CsSnI_3$, show promising J_{sc} values but often suffer from low V_{oc} (<1.0 V) and poor stability due to the rapid oxidation of Sn^{2+} to Sn^{4+}, limiting their efficiencies to around 17–20%.[52,54] Ge-based systems ($MAGeI_3$ and $FAGeI_3$) exhibit even lower efficiencies (7–22%) and lack environmental stability due to inherently weaker Ge–halide bonding and high defect densities.[50,51] Inorganic and chalcogenide alternatives like $BaZrS_3$ offer superior structural stability but currently display modest PCEs ($<10\%$) due to wider bandgaps and poor charge transport.[55] These limitations highlight the need for targeted defect passivation and film-quality improvement strategies. Importantly, the success of our chloride-doped $MAPbI_3$ devices suggests that similar halide engineering – particularly optimized chloride incorporation – could be applied to Pb-free perovskites to stabilize metal oxidation states, reduce trap density, and enhance crystallinity. Future work might therefore focus on exploiting chloride-assisted passivation in Sn- and Ge-based systems, improving interface engineering with stable inorganic transport layers, and adopting scalable, low-toxicity fabrication routes. Collectively, our strategies might apply in accelerating the development of environmentally benign, stable, and high-efficiency Pb-free perovskite SCs.

Conclusions

In summary, we have investigated a chlorine-doped perovskite solar cell with the device structure of ITO/ZnO(ETL)/perovskite-(active layer)/NiO_x(HTL)/Au. The active layer has been chosen to be $MAPbI_{3-x}Cl_x$ and the simulation was performed using the SCAPS-1D device modeling framework. First, we analyzed the performance parameters by varying the active-layer thickness to determine the optimal configuration. The results indicate that $MAPbI_3$ achieves its best performance at an absorber thickness of 800 nm, delivering a PCE of 24.17% with J_{sc} = 25.31 mA cm^{-2}, V_{oc} = 1.15 V and FF = 82.75%. Second, we investigated the impact of chlorine incorporation and found that $MAPbI_{2.8}Cl_{0.2}$ represents the most favorable composition, delivering a PCE of 27.34% with a J_{sc} of 25.00 mA cm^{-2}, a V_{oc} of 1.31 V, and an FF of 83.63%; this composition exhibits a higher V_{oc} than $MAPbI_{2.4}Cl_{0.6}$ because moderate chlorine incorporation efficiently passivates defects without inducing additional lattice strain or non-radiative recombination centers, whereas excessive Cl slightly degrades the V_{oc}. Finally, we compared our optimized device with previously reported structures utilizing various ETL, HTL, and absorber combinations to benchmark the performance improvements achieved through thickness and halide-composition optimization. Looking forward, these results not only demonstrate the promise of halide-modulated $MAPbI_3$ absorbers but also provide design guidance for emerging Pb-free perovskites. The optimization strategies established here can help overcome key challenges in Sn-, Ge-, Bi-, and double-perovskite systems and accelerate their development toward stable, high-efficiency, environmentally benign SCs.

Author contributions

M.A.K.S.: conceptualization, simulation, investigation, writing – original draft, writing – review & editing; M.S.I.: simulation, investigation, writing – review & editing, H.H.: supervision, resources, writing – review & editing, project administration, funding acquisition. All authors have read and agreed to the published version of the manuscript.

Conflicts of interest

The authors declare no competing financial interest.

Abbreviations

SCs	Solar cells
PV	Photovoltaic
PCE	Power conversion efficiency
PSCs	Perovskite solar cells
V_{oc}	Open circuit voltage
J_{sc}	Short circuit current density

Open Access Article. Published on 13 February 2026. Downloaded on 2/25/2026 7:33:26 AM.
This article is licensed under a Creative Commons Attribution-NonCommercial 3.0 Unported Licence.

FF	Fill factor
ITO	Indium doped tin oxide
HTL	Hole transport layer
ETL	Electron transport layer
EQE	External quantum efficiency

Data availability

Detailed data for current research finding and studies are available from the corresponding author upon request.

Acknowledgements

This research is supported in part by the National Science Foundation (NSF) under Grant No. 1229523, and by the US Army Research Office W911NF-14-1-0100.

References

1 M. A. Green, E. D. Dunlop, J. Hohl-Ebinger, M. Yoshita, N. Kopidakis, K. Bothe, D. Hinken, M. Rauer and X. Hao, Solar cell efficiency tables (Version 64), *Prog. Photovoltaics*, 2024, **32**(7), 425–441, DOI: 10.1002/pip.3831.

2 NREL, *Best Research-Cell Efficiency Chart*, National Renewable Energy Laboratory, 2025.

3 N. D. Pham, V. T. Tiong, P. Chen, L. Wang, G. J. Wilson, J. Bell and H. Wang, Enhanced perovskite electronic properties via a modified lead(II) chloride Lewis acid–base adduct and their effect in high-efficiency perovskite solar cells, *J. Mater. Chem. A*, 2017, **5**, 22954–22960, DOI: 10.1039/C6TA11139D.

4 S. Tombe, G. Adam, H. Heilbrunner, D. H. Apaydin, C. Ulbricht, N. S. Sariciftci, C. J. Arendse, E. Iwuoha and M. C. Scharber, Optical and electronic properties of mixed halide (X = I, Cl, Br) methylammonium lead perovskite solar cells, *J. Mater. Chem. C*, 2017, **5**, 1714–1723, DOI: 10.1039/C6TC04830G.

5 W. Shockley and H. J. Queisser, Detailed balance limit of efficiency of p-n junction solar cells, *J. Appl. Phys.*, 1961, **32**, 510–519, DOI: 10.1063/1.1736034.

6 L. K. Ono, E. J. Juarez-Perez and Y. Qi, Progress on perovskite materials and solar cells with mixed cations and halide anions, *ACS Appl. Mater. Interfaces*, 2017, **9**(36), 30197–30246, DOI: 10.1021/acsami.7b06001.

7 A. Kojima, K. Teshima, Y. Shirai and T. Miyasaka, Organometal halide perovskites as visible-light sensitizers for photovoltaic cells, *J. Am. Chem. Soc.*, 2009, **131**(17), 6050–6051.

8 S. Singh, R. Abdur, M. A. K. Sheikh, B. S. Swain, J. Song, J. H. Kim, H. S. Nam, S. H. Kim, H. Lee and J. Lee, Selective spin dewetting for perovskite solar modules fabricated on engineered Au/ITO substrates, *Nanomaterials*, 2024, **14**(5), 424, DOI: 10.3390/nano14050424.

9 B. S. Swain, M. A. K. Sheikh, S. Singh, R. Abdur, D. Jeong and J. Lee, $CH_3NH_3PbBr_3$ nanocubes-array for solar cell application, *Mater. Sci. Semicond. Process.*, 2018, **74**, 361–368, DOI: 10.1016/j.mssp.2017.10.050.

10 A. Yi, S. Chae, H. M. Luong, S. H. Lee, H. Lee, H. Yoon, D.-H. Kim, H. J. Kim and T.-Q. Nguyen, Room-temperature-processed perovskite solar cells surpassing 24% efficiency, *Joule*, 2024, **8**(7), 2087–2104, DOI: 10.1016/j.joule.2024.04.002.

11 M. Afroz, R. K. Ratnesh, S. Srivastava and J. Singh, Perovskite solar cells: Progress, challenges, and future avenues to clean energy, *Sol. Energy*, 2025, **287**, 113205, DOI: 10.1016/j.solener.2024.113205.

12 R. Abdur, S. Singh, M. A. K. Sheikh, M. A. A. Shaikh, M. S. Jamal and J. Lee, Modified post-annealing process with N, N-dimethylformamide vapor to control the growth of hybrid perovskite microstructure, *Results Mater.*, 2022, **16**, 100330, DOI: 10.1016/j.rinma.2022.100330.

13 D. B. Straus, S. Guo, A. M. Abeykoon and R. J. Cava, Understanding the instability of the halide perovskite $CsPbI_3$ through temperature-dependent structural analysis, *Adv. Mater.*, 2020, **32**(32), e2001069, DOI: 10.1002/adma.202001069.

14 G. Niu, X. Guo and L. Wang, Review of recent progress in chemical stability of perovskite solar cells, *J. Mater. Chem. A*, 2015, **3**, 8970–8980, DOI: 10.1039/C4TA04994B.

15 J. Hieulle, X. Wang, C. Stecker, D.-Y. Son, L. Qiu, R. Ohmann, L. K. Ono, A. Mugarza, Y. Yan and Y. Qi, Unraveling the impact of halide mixing on perovskite stability, *J. Am. Chem. Soc.*, 2019, **141**(8), 3515–3523, DOI: 10.1021/jacs.8b11210.

16 M. A. K. Sheikh, R. Abdur, S. Singh, J.-H. Kim, K.-S. Min, J. Kim and J. Lee, Efects of chlorine contents on perovskite solar cell structure formed on CdS electron transport layer probed by Rutherford Backscattering, *Electron. Mater. Lett.*, 2018, **14**, 700–711, DOI: 10.1007/s13391-018-0084-4.

17 X. Xu, Z. Zhang, T. Liu, P. Zhu, Z. Zhang and G. Xing, Suppressing the penetration of 2D perovskites for enhanced stability of perovskite solar cells, *J. Mater. Chem. A*, 2025, **13**, 12097–12103, DOI: 10.1039/d4ta08811e.

18 L. Zhu, S. Xu, G. Liu, L. Liu, H. Zhou, Z. Ai, X. Pan and F. Zhang, Engineering the passivation routes of perovskite films towards high performance solar cells, *Chem. Sci.*, 2024, **15**, 5642–5652, DOI: 10.1039/d3sc06746g.

19 Q. Wang, X. Zheng, Y. Deng, J. Zhao, Z. Chen and J. Huang, Stabilizing the α-phase of $CsPbI_3$ perovskite by sulfobetaine Zwitterions in one-step spin-coating films, *Joule*, 2017, **1**(2), 371–382, DOI: 10.1016/j.joule.2017.07.017.

20 Y. Jiang, L. Qiu, E. J. Juarez-Perez, L. K. Ono, Z. Hu, Z. Liu, Z. Wu, L. Meng, Q. Wang and Y. Qi, Reduction of lead leakage from damaged lead halide perovskite solar modules using self-healing polymer-based encapsulation, *Nat. Energy*, 2019, **4**(7), 585–593, DOI: 10.1038/s41560-019-0406-2.

21 Q. Chen, H. Zhou, Y. Fang, A. Z. Stieg, T.-B. Song, H.-H. Wang, X. Xu, Y. Liu, S. Lu and J. You, *et al.*, The optoelectronic role of chlorine in $CH_3NH_3PbI_3$(Cl)-based perovskite solar cells, *Nat. Commun.*, 2015, **6**, 7269, DOI: 10.1038/ncomms8269.

 © 2026 The Author(s). Published by the Royal Society of Chemistry

Open Access Article. Published on 13 February 2026. Downloaded on 2/25/2026 7:33:26 AM.
This article is licensed under a Creative Commons Attribution-NonCommercial 3.0 Unported Licence.

22 K. H. Stone, A. Gold-Parker, V. L. Pool, E. L. Unger, A. R. Bowring, M. D. McGehee, M. F. Toney and C. J. Tassone, Transformation from crystalline precursor to perovskite in $PbCl_2$-derived $MAPbI_3$, *Nat. Commun.*, 2018, **9**, 3458, DOI: 10.1038/s41467-018-05937-4.

23 M. Burgelman, P. Nollet and S. Degrave, Modelling polycrystalline semiconductor solar cells, *Thin Solid Films*, 2000, 527–532, DOI: 10.1016/S0040-6090(99)00825-1.

24 Y. Raoui, H. E. Zahraouy, N. Tahiri, O. E. Bounagui, S. Ahmad and S. Kazim, Performance analysis of $MAPbI_3$ based perovskite solar cells employing diverse charge selective contacts: Simulation study, *Sol. Energy*, 2019, **193**, 948–955, DOI: 10.1016/j.solener.2019.10.009.

25 M. Jamil, A. Ali, K. Mahmood, M. I. Arshad, S. Tahir, M. A. U. Nabi, S. Ikram, N. Amin and S. Hussain, Numerical simulation of perovskite/$Cu_2Zn(Sn_{1-x}Ge_x)S_4$ interface to enhance the efficiency by valence band offset engineering, *J. Alloys Compd.*, 2020, **821**, 153221, DOI: 10.1016/j.jallcom.2019.153221.

26 K. Bhavsar and P. B. Lapsiwala, Numerical simulation of perovskite solar cell with different material as electron transport layer using SCAPS-1D software, *Semicond. Phys., Quantum Electron. Optoelectron.*, 2021, **24**(3), 341–347, DOI: 10.1016/j.ijoes.2024.100893.

27 Y. Song, L. Yan, Y. Zhou, B. Song and Y. Li, Lowering the work function of ITO by covalent surface grafting of aziridine: application in inverted polymer solar cells, *Adv. Mater. Interfaces*, 2015, **2**, 1400397, DOI: 10.1002/admi.201400397.

28 P. Sawicka-Chudy, Z. Starowicz, G. Wisz, R. Yavorskyi, Z. Zapukhlyak, M. Bester, Ł. Głowa, M. Sibiński and M. Cholewa, Simulation of TiO_2/CuO Solar Cells with SCAPS-1D Software, *Mater. Res. Express*, 2019, **6**, 085918, DOI: 10.1088/2053-1591/ab22aa.

29 M. I. Hossain, F. H. Alharbi and N. Tabet, Copper oxide as inorganic hole transport material for lead halide perovskite based solar cells, *J. Sol. Energy*, 2015, **120**, 370–380, DOI: 10.1016/j.solener.2015.07.040.

30 F. Anwar, R. Mahbub, S. S. Satter and S. M. Ullah, Effect of different HTM layers and electrical parameters on ZnO nanorod-based lead-free perovskite solar cell for high-efficiency performance, *J. Spectrosc.*, 2017, 9846310, DOI: 10.1155/2017/9846310.

31 Q. Zhou, D. Jiao, K. Fu, X. Wu, Y. Chen, J. Lu and S. Yang, Two-dimensional device modeling of $CH_3NH_3PbI_3$ based planar heterojunction perovskite solar cells, *Sol. Energy*, 2016, **123**, 51–56, DOI: 10.1016/j.solener.2015.11.009.

32 S. Chaudhary, V. Yadav, C. M. S. Negi and S. K. Gupta, Active layer thickness dependence of optoelectronic performance in $CH_3NH_3PbI_3$ perovskite-based planar heterojunction photodiodes, *Opt. Mater.*, 2020, **106**, 109960, DOI: 10.1016/j.optmat.2020.109960.

33 B. Zhang, M.-J. Zhang, S.-P. Pang, C.-S. Huang, Z.-M. Zhou, D. Wang, N. Wang and G.-L. Cui, Carrier transport in $CH_3NH_3PbI_3$ films with different thickness for perovskite solar cells, *Adv. Mater. Interfaces*, 2016, **3**, 1600327, DOI: 10.1002/admi.201600327.

34 M. S. Mahmood and N. K. Hassan. Simulation of a perovskite sandwich solar cell with the p-CZTS/p-CH3 NH3PbCI3/p-CZTS absorber layers. IOP Conference Series: Earth and Environmental Science, 2021, 877, 012001, DOI: 10.1088/1755-1315/877/1/012001.

35 G. A. Nowsherwan, Q. Ali, N. Nowsherwan, U. F. Ali and S. S. Hussain, Performance and stability improvements in $MAPbI_3$ perovskite photovoltaics with $CsPbI_3$ quantum dots, *Multiscale Multidiscip. Model. Exp. Des.*, 2025, **8**, 10, DOI: 10.1007/s41939-024-00584-3.

36 A. Zekry, I. Yahyaoui and F. Tadeo, Generic Analytical Models for Organic and Perovskite Solar Cells. 10th International Renewable Energy Congress (IREC) (IEEE, Sousse, Tunisia) 2019, 1–6, DOI: 10.1109/IREC.2019.8754574.

37 N. Shahadath, M. A. B. Siddique, M. Tarekuzzaman, M. H. Ishraq, M. F. Rahman, A. M. Arfi, M. Rasheduzzaman, S. M. G. Mostafa and M. Z. Hasan, Optimization of high efficiency lead-free double perovskite Dy_2NiMnO_6 (DNMO) for optimal solar cell and renewable energy applications: a numerical SCAPS-1D simulation, *New J. Chem.*, 2024, **48**, 14336–14353, DOI: 10.1039/D4NJ02754J.

38 M. K. Hossain, M. S. Uddin, G. F. I. Toki, M. K. A. Mohammed, R. Pandey, J. Madan, M. F. Rahman, M. R. Islam, S. Bhattarai and H. Bencherif, *et al.*, Achieving above 24% efficiency with non-toxic $CsSnI_3$ perovskite solar cells by harnessing the potential of the absorber and charge transport layers, *RSC Adv.*, 2023, **13**, 23514–23537, DOI: 10.1039/D3RA02910G.

39 A. Kanoun, M. B. Kanoun and A. E. Merad, Toward development of high-performance perovskite solar cells based on $CH_3NH_3GeI_3$ using computational approach, *Sol. Energy*, 2019, **182**, 237–244, DOI: 10.1016/j.solener.2019.02.041.

40 M. R. Iftekhar; M. G. Rabbani; A. Hosen; M. S. Islam; M. S. Mian and S. R. Al Ahmed, Simulating the electrical characteristics of a highly efficient $Cs_2AgBiBr_6$-based perovskite solar cell with NiO_x hole transport layer International Conference on Advancement in Electrical and Electronic Engineering (ICAEEE) 2022, 1–4., DOI: 10.1109/ICAEEE54957.2022.9836484.

41 A. Mortadi, E. M. El Hafidi, H. Nasrellah, M. Monkade and R. El Moznine, Investigation of bandgap grading on performances of perovskite solar cell using SCAPS-1D and impedance spectroscopy, *Sol. Energy Adv.*, 2024, **4**, 100056, DOI: 10.1016/j.seja.2024.100056.

42 Y. H. Khattak, F. Baig, A. Shuja, S. Beg and B. S. Soucase, Numerical analysis guidelines for the design of efficient novel nip structures for perovskite solar cell, *Sol. Energy*, 2020, **207**, 579–591, DOI: 10.1016/j.solener.2020.07.012.

43 M. K. Hossain, M. H. K. Rubel, G. F. I. Toki, I. Alam, M. F. Rahman and H. Bencherif, Effect of various electron and hole transport layers on the performance of $CsPbI_3$-Based perovskite solar cells: a numerical investigation in DFT, SCAPS-1D, *ACS Omega*, 2022, **7**, 43210–43230, DOI: 10.1021/acsomega.2c05912.

44 M. K. Hossain, G. F. I. Toki, A. Kuddus, M. H. K. Rubel, M. M. Hossain, H. Bencherif, M. F. Rahman, M. R. Islam

Open Access Article. Published on 13 February 2026. Downloaded on 2/25/2026 7:33:26 AM.
This article is licensed under a Creative Commons Attribution-NonCommercial 3.0 Unported Licence.

and M. Mushtaq, An extensive study on multiple ETL and HTL layers to design and simulation of high-performance lead-free $CsSnCl_3$-based perovskite solar cells, *Sci. Rep.*, 2023, **13**, 2521, DOI: 10.1038/s41598-023-28506-2.

45 M. S. Reza, A. Ghosh, A. Gassoumi, M. R. Hasan, M. Shahjalal, A. K. M. Yahia, M. S. Reza, R. K. Prodhan, M. M. Islam and M. J. Talukder, *et al.*, A comprehensive investigation involving numerous HTL and ETL layers to design and simulate high-efficiency Ca_3AsI_3-based perovskite solar cells, *Inorg. Chem. Commun.*, 2025, **172**, 113647–113669, DOI: 10.1016/j.inoche.2024.113647.

46 A. M. Elseman, A. E. Shalan, M. M. Rashad and A. M. Hassan, Experimental and simulation study for impact of different halides on the performance of planar perovskite solar cells, *Mater. Sci. Semicond. Process.*, 2017, **66**, 176–185, DOI: 10.1016/j.mssp.2017.04.022.

47 A. Varadwaj; P. R. Varadwaj and K. Yamashita. Unraveling a structure-property relationship for methylammonium lead/tin trihalide organic-inorganic hybrid perovskite solar cells. arXiv:1703.10914 [cond-mat.mtrl-sci.], 2017, DOI: 10.48550/arXiv.1703.10914.

48 J. Laali, A. Hamedani, G. Alahyarizadeh and A. Minuchehr, Performance analysis of the perovskite solar cells by a realistic, DFT-accurate optical absorption spectrum, *Superlattices Microstruct.*, 2020, **143**, 106551, DOI: 10.16/j.spmi.2020.106551.

49 N. Bouri, A. Talbi, Y. Khaaissa, S. Derbali, A. Bouich and K. Nouneh, Insight into $MAPb_{1-x}Eu_xI_3$ based perovskite solar cell performance using SCAPS Simulator, *Optik*, 2022, **271**, 170235, DOI: 10.1016/j.ijleo.2022.170235.

50 A. Ferdous and G. Hashmi, A comprehensive device modeling of organic-inorganic hybrid $CH_3NH_3GeI_3$ based perovskite solar cell, *Results Mater.*, 2025, **25**, 100665, DOI: 10.1016/j.rinma.2025.100665.

51 M. Mehrabian, M. Taleb-Abbasi and O. Akhavan, Using Cu_2O/ZnO as two-dimensional hole/electron transport nanolayers in unleaded $FASnI_3$ perovskite solar cells, *Materials*, 2024, **17**(5), 1064, DOI: 10.3390/ma17051064.

52 S. Lin, B. Zhang, T.-Y. Lü, J.-C. Zheng, H. Pan, H. Chen, C. Lin, X. Li and J. Zhou, Inorganic lead-free B-γ-$CsSnI_3$ perovskite solar cells using diverse electron-transporting materials: A simulation study, *ACS Omega*, 2021, **6**, 26689–26698, DOI: 10.1021/acsomega.1c04096.

53 S. M. Hasnain, A. Iqbal, I. Qasim, K. Irshad, M. A. Mir, M. I. Malik and L. S. Sundarf, Performance evaluation of organometal halide $MASnI_3$ and inorganic $BaZrS_3$ hybrids in perovskites solar cells: Theoretical approach, *Hybrid Adv.*, 2025, **9**, 100408, DOI: 10.1016/j.hybadv.2025.100408.

54 Q. Li, W. Wan, Y. Ge, B. Wang, Y. Li, C. Wang, Y.-H. Zhao and Y. Liu, Hexagonal $MASnI_3$ exhibiting strong absorption of ultraviolet photons, *Appl. Phys. Lett.*, 2019, **114**(10), 101906, DOI: 10.1063/1.5087649.

55 X. Wei, H. Hui, S. Perera, A. Sheng, D. F. Watson, Y.-Y. Sun, Q. Jia, S. Zhang and H. Zeng, Ti-alloying of $BaZrS_3$ chalcogenide perovskite for photovoltaics, *ACS Omega*, 2020, **24**(5), 18579–18583, DOI: 10.1021/acsomega.0c00740.

 © 2026 The Author(s). Published by the Royal Society of Chemistry